university of groningen

University Medical Center Groningen

University of Groningen

X-ray analysis of protective coatings

Zoestbergen, Edzo

IMPORTANT NOTE: You are advised to consult the publisher's version (publisher's PDF) if you wish to cite from it. Please check the document version below.

Document Version
Publisher's PDF, also known as Version of record

Publication date:
2000

Link to publication in University of Groningen/UMCG research database

Citation for published version (APA):
Zoestbergen, E. (2000). *X-ray analysis of protective coatings*. s.n.

Copyright
Other than for strictly personal use, it is not permitted to download or to forward/distribute the text or part of it without the consent of the author(s) and/or copyright holder(s), unless the work is under an open content license (like Creative Commons).

The publication may also be distributed here under the terms of Article 25fa of the Dutch Copyright Act, indicated by the “Taverne” license. More information can be found on the University of Groningen website: https://www.rug.nl/library/open-access/self-archiving-pure/taverne-amendment.

Take-down policy
If you believe that this document breaches copyright please contact us providing details, and we will remove access to the work immediately and investigate your claim.

Downloaded from the University of Groningen/UMCG research database (Pure): http://www.rug.nl/research/portal. For technical reasons the number of authors shown on this cover page is limited to 10 maximum.

Download date: 18-04-2025

2 Fundamentals

2.1 Sputtering

Introduction

The sputter-erosion of solid material by positive ion bombardment is widely used as a source of vapour for thin film deposition [1,2]. In comparison with other techniques, sputtering has some advantages; any material can be volatilised, compounds are volatilised stochiometrically and film deposition rates can be made uniform over large areas. Furthermore the kinetic energy of sputtered atoms falls largely within the energy range for displacing of surface atoms without causing subsurface damage. In addition, sputter erosion of the film, as it is being deposited, can be used to improve film coverage over rough topography, to enhance the preferential crystallographic orientation of the deposit and to affect the residual stresses in the deposit.

There are several techniques available to generate the necessary positive inert gas ions for sputtering. However, one of the easiest methods is by establishing a glow discharge plasma. The plasma is used to couple non-thermal energy from an electric field into the film deposition process. The plasma generation starts with the acceleration of free electrons in an applied electric field. If the kinetic energy of the electrons is high enough electron impact reactions with gas molecules will generate electrons, free radicals, excited-state molecules and ions. Due to the voltage drop between the target and the plasma, generated by the biased target, ions are accelerated out of he plasma into the target. Figure 2.1 shows schematically the set-up of a sputter unit.

Besides the inert gas ions that leave the plasma other energetic particles, will diffuse out of the plasma towards the containment walls and film surface. The steady state concentration of each type of particle within the plasma represents a balance between its generation and loss rate. The plasma can be divided in two areas; the bulk centre plasma and the boundary region, called sheath region. The plasma behaviour in the sheath region is crucial both for sustaining the plasma and to control the film deposition. Therefore, the plasma plays an important role in the deposition process and has a large influence on the deposit obtained.

The positive gas ions are bombarding the target and the cathode material is the material of which a film is formed. However, the intentional inclusion of a

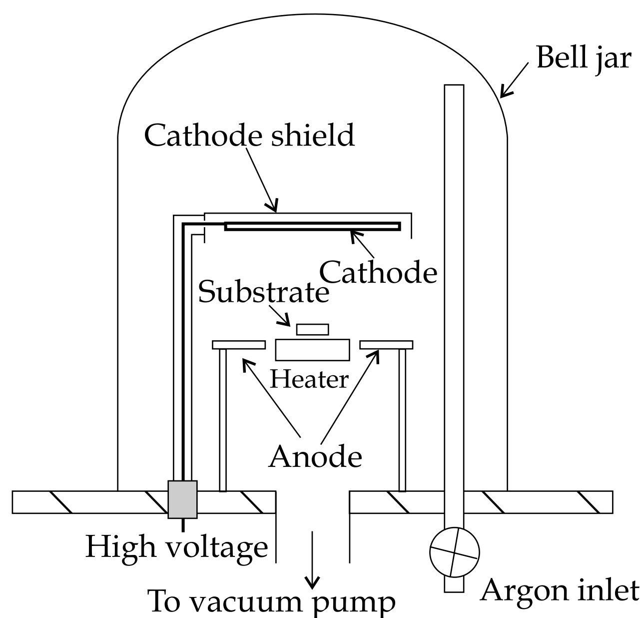

Figure 2.1 General set-up of a sputter deposition chamber

reactive gas in the sputter atmosphere enables one to alter or control the properties of the deposit. This is called reactive sputtering. The exact mechanism by which compounds are formed during reactive sputtering is not yet known. Depending on the pressure of the reactive gas, a reaction may occur during the deposition of the film either at the cathode or at the surface. In most cases, the composition of the film may be altered by simply varying the proportion of reactive to inert gases in the discharge.

The properties of the deposit can be seriously affected by the choice of the particular conditions used for sputtering. Besides the already mentioned plasma and ratio of reactive to inert gas, there are numerous other parameters that control the deposit. Examples are the used inert gases, the pressure in the deposition chamber, geometry of the chamber and the sputtering current and voltage. The influence of most of these parameters lies outside the scope of this thesis. However, there is one parameter that improves the film quality considerably. By also biasing the substrate negatively, ions may be accelerated out of the same plasma into the substrate to enhance resputtering. (When the substrate is electrically insulating radio frequency bias rather then DC bias must be used.) It is believed that this ion bombardment removes absorbed gases and badly adherent particle and consequently films of higher purity are produced. Furthermore, the bombardment of the deposit may influence the state of stress and the crystallographic orientation of the films.

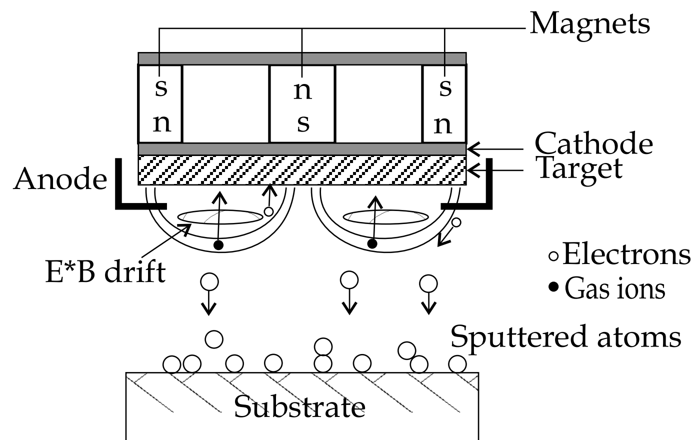

Figure 2.2 Specific set-up for plasma enhanced sputter deposition

2.1.1 Magnetron sputtering

Magnetron sputtering is an enhanced sputter method, which enables a higher deposition rate at low operating pressure together with the possibility to obtain high quality films at low substrate temperatures. This is achieved by applying a magnetic field perpendicular to the electric field of the target electrons (Figure 2.2). Electrons are forced to follow a closed drift path caused by the crossed fields, i.e. the electrons are trapped in a channel. The effect of this is twofold:

- The number of ionised argon atoms will increase significantly allowing a lower argon pressure
- An increase of the mean free path, which is inversely proportional to the pressure.

The outcome is a higher field of particles on the substrate at a lower pressure, which has a positive influence on the quality of the deposit.

Preparation of the magnetron sputtered films

The magnetron sputtered TiN films that are studied in chapter 3 and 4 of this thesis were manufactured at the University of Technology of Eindhoven [3].

The TiN deposits were fabricated in a Teer UDP 350 4-RF DC system. The deposition chamber has a cylindrical shape with a diameter and a height of 0.5m. Two facing titanium targets, dimensions 130×240 mm, are aligned along the side of the deposition chamber. Between the two targets a rotating drum is placed onto which the specimens are mounted. The drum rotates with a speed of 5 rpm. When the specimens on the drum are facing a target the distance between the target and the specimen is approximately 130 mm.

The base pressure in the chamber is $6.65 \cdot 10^{-4}$ Pa. Next, the chamber is filled with argon until the pressure is 0.4 Pa. The specimens were cleaned by means of sputtering during 30 minutes at a bias voltage of –1000 V and a current of 0.2 Ampere. During this cleaning the substrate temperature is slowly increased to 620 K. After the substrate is sufficiently cleaned, a pure Ti interlayer with a thickness of approximately 200 nm is deposited at a bias voltage of –150 V and a current of 7.5 Ampere. Finally, nitrogen is admitted into the chamber and the bias voltage is adjusted to the desired value.

To determine the particle density of a specific element in the plasma, one can measure its emission. The intensity of the emission during sputtering of pure titanium is defined as 100%. By leading nitrogen into the chamber the density of titanium in the plasma will decrease and as a result a lower intensity will be measured. The actual amount of nitrogen injected into the chamber will influence the stoichiometry of the films. A stoichiometric TiN film was attained by a titanium concentration ranging between 55 and 60%.

In total, three different batches are prepared:

- In the first batch the bias voltage was kept to –40 Volt, and the titanium concentration was varied.
- For the second batch the Ti concentration was held constant at 55%, but the deposition time was varied at a bias voltage of -65 Volt.
- The third set of specimens was prepared at a bias voltage of –80 Volt and again the titanium concentration was varied. In the first and third batch the titanium concentration was varied from 40 to 80 % and the deposition time was 60 minutes.

All the layers are deposited onto WC based cermet cuboids of dimensions 20×20×3 mm. The three batches and the deposition parameters are tabulated in Table 2.1.

Table 2.1 The magnetron sputtered TiN specimens.

	Batch 1					
Bias voltage [V]	-40	-40	-40	-40	-40	-40
Deposition time [min]	60	60	60	60	60	60
Titanium concentration [%]	40	50	55	60	70	80
	Batch 2					
Bias voltage [V]	-65	-65	-65	-65		
Deposition time [min]	30	45	60	90		
Titanium concentration [%]	55	55	55	55		
	Batch 3					
Bias voltage [V]	-80	-80	-80	-80	-80	-80
Deposition time [min]	60	60	60	60	60	60
Titanium concentration [%]	40	50	55	60	70	80

2.1.2 Commercial PVD films

PVD, physical vapour deposition, is a generic term used for all the different deposition techniques for which the generation of a vapour, using a physical process, forms the base. The above-mentioned magnetron sputtering and vacuum evaporation are two examples of PVD techniques.

Balzers using a standard commercial process fabricated the PVD films investigated in chapter 5 and 6. Three different refractory hard films are studied:

1. TiN
2. Ti(C,N)
3. A multi-layer system of alternating TiN and TiAlN sub-layers.

In the first batch films are deposited onto two different substrates:

1. AISI304 stainless steel
2. AISI D2 tool steel.

The substrates had a thickness of 1 mm, a surface area of 10 by 90 mm and the surface roughness of the bare substrates was 0.03 µm R_a.

In the second batch the influence of the pre-treatment on the characteristics of the films was studied. This was achieved by depositing the different films on tool steel substrates, AISI D2, with a varying substrate roughness; 1 µm, 0.1 µm and 0.01 µm R_a. The substrate dimensions were $2\times10\times44$ mm^3. These dimensions are chosen because of the in-situ bending experiments carried out in the FEG-XL30 ESEM. To be able to perform these in-situ bending experiments the length of the specimens should be between 42 and 48 mm.

2.1.3 Materials properties

The three ceramic coatings that are studied in this thesis all have the same Structurebericht designation: they all belong to the Fm3m space group. There is also a large similarity in their physical properties.

There are three different titanium nitrides; a tetragonal nitride, Ti_2N, the bct nitride, δ', and the fcc nitride, TiN [4]. This last nitride exists over a large nitride range, from 28 to >50 atom% N, and has the already mentioned Fm3m space group, i.e. NaCl prototype.

The type of bonding in the fcc nitride is characterised by partly covalent and partly metallic [5] and the exact nature is largely influenced by the exact chemical composition. This is visible in the data that are available for the Young's modulus, Poisson's ratio and the elastic compliances [6,7,8,9]. Young's modulus ranging from 256 to 640 GPa are reported and the anisotropy factor

ranging from 1 to 0.5, that is respectively isotropic and anisotopic. The anisotropy factor of a cubic material is defined by $2*(S_{11}-S_{12})/S_{44}$, if this value is equal to 1 the material is elastically isotropic. The mixed nature is also visible in the hardness and the electrical resistance. TiN is much harder than titanium but the electrical resistance of TiN is lower than that of pure titanium, Ti≈$80\text{-}42\cdot10^{-6}$ Ωcm and TiN≈$12\cdot10^{-6}$ Ωcm. Regardless of the uncertainty, some of the physical properties of TiN and of the other systems are summarised in Table 2.2 [10,11,12,13].

Table 2.2 Properties of the used coatings

	Material		
Physical properties	TiN	TiC	TiAlN
Mol wt.	61.91	59.91	
Density [g cm^{-3}]	5.22	4.93	
Melting temperature [K]	3203	3413±90	2473-3203
Thermal expansion [10^{-6} K]	8.6	8.6	7.5
Specific heat [J kg^{-1} K^{-1}]	630	557	
Lattice spacing [Å]	4.2392^{+}	4.3274	4.1700
	$TiN_{0.7}C_{0.3}$ 4.2971		
Heat of formation [J mole^{-1}]	$-3.4\cdot10^{5}$	$-1.9\cdot10^{5}$	
Free energy [J mole^{-1}]	$-3.1\cdot10^{5}$	$-1.8\cdot10^{5}$	
Bond strength	111	104	
D_0^{++} [cm^2 sec]	$5.4\cdot10^{-3}$	0.14	
Activation energy for diffusion, Q^{++} [[J mole^{-1}]	$2.2\cdot10^{8}$	$2.3\cdot10^{8}$	
Hardness [Hv]	2950	3200	3450
Young's modulus [GPa]	250-600	450	450
Poisson's ratio	0.2-0.3	0.23	
Electrical resistance [Ω cm]	$0.1152\cdot10^{-4}$	$1.93\cdot10^{-4}$	

$^{+}$Depending on the nitrogen concentration.
$^{++}$Self diffusion of N in TiN

For TiC there are two distinct phases: TiC for 32 to 48.8 atom% C and Ti_2C for 32 to 36 atom% C in which the vacancies are ordered on the sub-lattice. The physical data for TiC are less indistinct than those of TiN. This may be partly a consequence of the bonding, which is more covalent than TiN. TiC has not only a higher hardness than TiN but the electrical resistance is also much higher.

During vapour deposition it is possible to obtain a stable $Ti_{1-x}Al_xN$ deposit with a NaCl type of structure. Aluminium concentrations up to x=0.6 can be achieved in this manner. The TiAlN coatings show an improvement in anti-oxidation properties in comparison with TiN. Oxidation of this system is not

observed during annealing in air at 973 K [14]. The TiAlN system shows also an increase in cutting performance in comparison with pure TiN coatings. The physical properties [15,16] that can be found in the literature about TiAlN are limited, probably due to the dependence on the exact chemical composition. However, some information about Fm3m AlN may be useful. AlN has a lattice spacing of 4.12 Å and with the data of TiN and Vegard's law it is possible to calculate the lattice spacing assuming the composition is known. The melting temperature of AlN is 2473 K and the T_{melt} of TiAlN is probably higher.

The composition and the thermal expansion coefficient of the used substrate materials are summarised in Table 2.3.

Table 2.3 Composition and expansion coefficient of the used substrates

	WC cermet	Tool steel	Stainless steel
Composition	WC grains in a Co matrix.	Fe +atom%: 1.55 C, 0.3 Si, 0.3 Mn, 12.0 Cr, 0.8 Mo, 0.8 V	Fe +atom%: Max 0.08 C, 1.0 Si, 19.0 Cr, 2.0 Mn, 10.0 Ni
Thermal expansion coefficient	$(4.6\text{-}8.9)\cdot 10^{-6}$	$(11.9\text{-}12.9)\cdot 10^{-6}$	$(17.8\text{-}18.4)\cdot 10^{-6}$

2.2 X-ray diffraction

Introduction

On November the 8th 1895, Wilhelm Röntgen's attention was drawn to a glowing fluorescent screen on a nearby table. Röntgen immediately determined that the fluorescence was caused by invisible rays originating from the partially

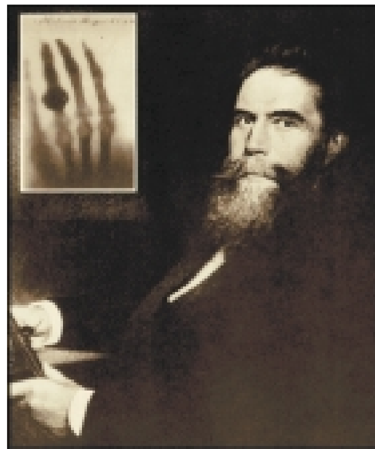

Figure 2.3 The discoverer of X-rays, Wilhelm Röntgen

evacuated glass tube he was using to study electrons. Surprisingly, these mysterious rays penetrated the opaque black paper wrapped around the tube. Röntgen, Figure 2.3, had discovered X-rays, the X because nothing was known about the radiation, a momentous event that instantly revolutionised the field of physics and medicine. For his discovery, Röntgen received the first Nobel Prize in physics in 1901. When later asked what his thoughts were at the moment of his discovery, he replied "I didn't think, I investigated."

2.2.1 Properties of X-rays

Nowadays the properties and nature of the unknown X-rays are completely charted [17,18,19]. We know that X-rays are electromagnetic radiation with exactly the same nature as visible light. The difference in wavelength, 0.5 – 2.5 Å for X-rays and 6000 Å for visible light, gives the impression of a different behaviour but this is just a deception.

X-rays may be excited in a number of ways. The primary X-rays generated in generators are produced by accelerating electrons in an evacuated chamber by an electric field. The electrons are then slowed down or stopped by collisions. During the deceleration of the electrons X-rays are emitted. If the energy of the bombarding electrons is sufficiently high, electron holes may be formed. If these holes are filled X-rays are emitted that will show sharp lines superposed on a continuous background. This emission spectrum possesses the specific characteristics of the matter that is hit by the electrons. In Figure 2.4 the

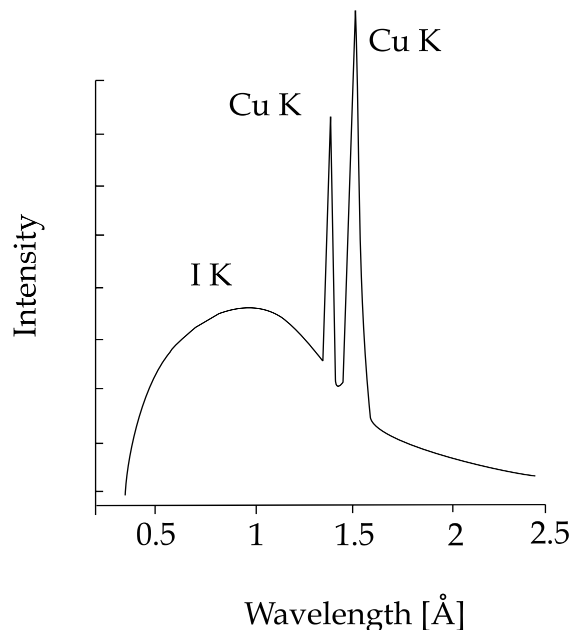

Figure 2.4 Emission spectrum of a Cu X-ray tube.

spectrum of Cu is presented showing three distinct emissions Kβ, $K\alpha_1$ and $K\alpha_2$. These emissions are generated when an electron decays to a lower shell and the wavelengths of the emission, i.e. energy, is determined by the energy difference between the shells participating in this process.

X-rays are generated when electrons interact with matter but what happens when an X-ray interacts with matter, in this case an atom?

- The reverse process that occurs during production of the X-ray may take place, the X-ray is absorbed and an electron of the atom is excited to a higher shell.
- The X-ray may be scattered from electrons of the atom.

There are two kinds of scattering: unmodified scattering (same wavelength) and Compton modified scattering (longer wavelength). The modified scattering from the different electrons is completely incoherent because there is a change in wavelength. It produces a diffuse background and is therefore of no further use. We are only interested in the monochromatic unmodified scattering. The intensity of classical scattering by a single free electron is:

$$I_e = I_0 \cdot \frac{1}{(4\pi\varepsilon_0)^2} \cdot \frac{e^4}{m^2 c^4 R^2} \cdot \left(\frac{1+\cos^2\phi}{2} \right) \tag{2.1}$$

(with e and m the electron charge and mass, R the distance between the point of observation and scattering and ϕ the angle between the incident and the diffracted beam.) To obtain the scatter interaction of an X-ray with an atom it is necessary to consider the different electrons of an atom. The amplitude of the unmodified scattering per atom is the sum of the amplitudes per electron.

Knowing the scattering factor of an individual atom enables us to derive the interaction of X-rays with a crystal. The amplitude of scattering from an atom was the sum of the amplitudes per electron and the scattering by a crystal is the sum of the amplitudes per atom. The only difference is that for a crystalline material the positions of the atoms are more or less fixed, unlike the electrons. This necessitates the addition of a structure factor to the summation, to consider the spatial distribution of the atoms within a unit cell. However, a crystal is composed of multiple unit cells, which have a periodic distribution in space, resulting in, just as for the unit cell, an additional summation over all the unit cells in the crystal.

The diffraction from a unit cell is depicted in Figure 2.5 where O is the position of the unit cell's origin. If the distance between the point of observation and O is relatively large with respect to the distance between the points of scattering this difference can be neglected, i.e. $x_2=x_2'$. The structure factor, using Fourier space, is then a complex exponential. The exponent is given by the difference between

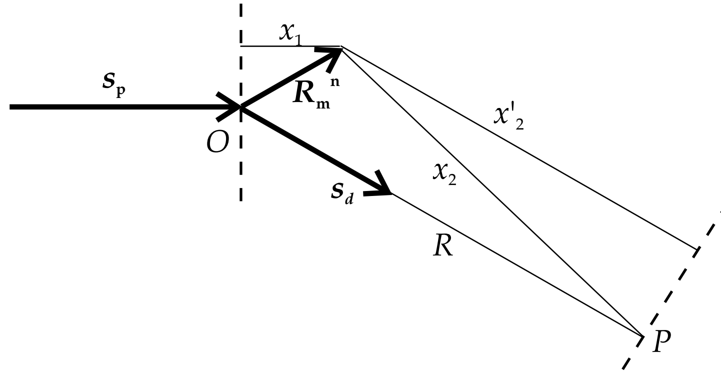

Figure 2.5 X-ray waves in reciprocal space

primary and diffracted beams times the position of the atoms relative to the cell origin summed over the atoms in a unit cell.

$$F = \sum_{n} f_n \cdot \mathrm{e}^{(2\pi i/\lambda)\cdot(\vec{s_d}-\vec{s_p})\cdot r_n} \tag{2.2}$$

where λ is the wavelength of the X-ray, s_p and s_d are the unit vectors in the directions of the primary and diffracted beams and r_n are the positions of the atoms within the unit cell. The mathematical representation for the periodicity of unit cells in the crystals has exactly the same shape as the structure factor:

$$H_i = \sum_{m_i=0}^{N_i-1} \mathrm{e}^{(2\pi i/\lambda)\cdot(\vec{s_d}-\vec{s_p})\cdot m_i\vec{a_i}} = \frac{\mathrm{e}^{(2\pi i/\lambda)\cdot(\vec{s_d}-\vec{s_p})\cdot N_i\vec{a_i}}-1}{\mathrm{e}^{(2\pi i/\lambda)\cdot(\vec{s_d}-\vec{s_p})\cdot\vec{a_i}}-1} \tag{2.3}$$

(N_i is the number of unit cells along the direction $\mathbf{a}_i$.) The instantaneous field is now simply obtained by the product of the two geometry factors and the scattering from an individual atom:

$$E = \frac{1}{4\pi\varepsilon_0}\cdot\frac{E_0 e^2}{mc^2 R}\mathrm{e}^{2\pi i[\nu t-(R/\lambda)]}\cdot F\times H_1\times H_2\times H_3 \tag{2.4}$$

The intensity of an unpolarized primary beam scattered from a crystal is obtained by multiplying the instantaneous field with its complex conjugated resulting in:

$$I = I_e \cdot F^2 \sum_{i=1}^{3} \frac{\sin^2(\pi/\lambda)\cdot(\vec{s_d}-\vec{s_p})\cdot N_i\vec{a_i}}{\sin^2(\pi/\lambda)\cdot(\vec{s_d}-\vec{s_p})\cdot\vec{a_i}} \tag{2.5}$$

This harmonic function may be represented by $\sin^2 Nx$. Assuming that N is very large results in a function that is zero except in the vicinity of $x=n\pi$. This condition is satisfied when three conditions are simultaneously fulfilled:

$$\left(\frac{\pi}{\lambda}\right)\cdot\left(\overrightarrow{s_d}-\overrightarrow{s_p}\right)\cdot\overrightarrow{a_1}=h'\pi \quad (a)$$
$$\left(\frac{\pi}{\lambda}\right)\cdot\left(\overrightarrow{s_d}-\overrightarrow{s_p}\right)\cdot\overrightarrow{a_2}=k'\pi \quad (b) \qquad (2.6)$$
$$\left(\frac{\pi}{\lambda}\right)\cdot\left(\overrightarrow{s_d}-\overrightarrow{s_p}\right)\cdot\overrightarrow{a_3}=l'\pi \quad (c)$$

These equations are know as the 3 von Laue equations and were derived by von Laue in 1912. They express the necessary conditions for diffraction. The three Laue equations can be written in a much easier mathematical form as formulated by Bragg. His law states that when the difference in path length experienced by radiation scattered from two adjacent lattice planes is equal to the wavelength of the radiation or a multiple of this, constructive interference will occur.

$$n\lambda = 2d\cdot\sin\theta \qquad (2.7)$$

The advantage of this law is that it is very simple and easy to derive. However, there are also some advantages using the Laue equations. The size of the crystals has an influence on the width of the diffraction peak, which is not apparent from Bragg’s law, and the intensity is linearly proportional to the number of unit cells that have the same orientation. So X-ray diffraction can not only be used to determine the structure factor of a material or the lattice spacing, but it may also provide valuable information concerning the size and crystallographic orientation of crystallites.

A relevant question to address is:” What is the information area that is investigated using X-rays?” To answer this question it is once again necessary to study the interaction of X-rays with matter:

- The emission of an electron, this fraction of energy subtracted from the beam is called true absorption.
- Inelastic scattering, which becomes significant for elements lighter than iron and for wavelengths shorter than 0.5 Å.

The equation for loss of intensity by these phenomena for monochromatic radiation is:

$$I_\lambda = I_0\,\mathrm{e}^{-\left(\frac{\mu}{\rho}\right)\rho z} \qquad (2.8)$$

(For a mass absorption coefficient (μ/ρ), density ρ, and path length z, I_0 is the initial intensity). For each element the mass absorption coefficient is different and a function of the wavelength. The range spanned by the different X-ray sources is approximately between 1 and 50 micrometer. The information obtained using X-ray diffraction is always an integrated average over the penetration depth.

The size of the surface area that is probed by the X-ray beam is determined by the size of the slits used during the diffraction experiments but is usually in the order of millimetres.

2.2.2 Determination of the lattice spacing

This section describes the accurate determination of lattice spacing of a cubic structure with d_0 [18]. This parameter may be determined using Bragg's law:

$$n\lambda = 2 d_{hkl} \sin\theta_{hkl} \tag{2.9}$$

with

$$d_{hkl} = \frac{d_0}{\sqrt{h^2 + k^2 + l^2}} \tag{2.10}$$

Consequently it is possible to determine d_0 from each reflection. The accuracy in d_0 is basically the accuracy with which θ and λ can be determined. Differentiating Bragg's law with respect to θ shows that the error in d_0 is proportional to $\cot\theta$. Therefore, the error in d_0, generated by a defined $\Delta\theta$, is smaller when a reflection at a higher 2θ angle is used.

Although there are different sources of systematic errors in d_0 the predominant source of error is displacement of the specimen from the diffractometer axis. This results in an error in the lattice spacing defined by:

$$\frac{\Delta d_0}{d_0} = -\frac{D}{R}\cos\theta\cot\theta \tag{2.11}$$

Where D is the horizontal displacement of the specimen from the diffractometer axis and R is the distance from the specimen to the detector. The procedure is now as follows:

- Determine d_0 for different {hkl} planes with Equation (2.10).
- Plot these data as a function of the $\cos\theta\cdot\cot\theta$ (called a Nelson-Riley plot).

Linear extrapolation to $\cos\theta\cdot\cot\theta=0$ gives a lattice spacing which takes the systematic errors in consideration. Deviations from the linear relation are due to the accuracy limit or are a result of the nature of the specimen.

2.2.3 X-rays and crystallographic orientation

In most polycrystalline specimens the individual crystals exhibit a spatial alignment, which is known as a *preferred orientation* or *crystallographic texture* [19]. Such an alignment will impart a degree of anisotropy on the physical properties depending on the anisotropy in single crystal properties. It is possible using X-ray diffraction to determine this preferred orientation. This is because Equation (2.5) states that the intensity is linearly proportional to the amount of crystals oriented with a specific alignment. With the reflection method of Schultz it is possible to perform these measurements. The procedure is to mount the specimen on a platform that has its normal perpendicular to the diffractometer axis. A 2θ angle is chosen in order to satisfy the necessary diffraction conditions. The platform is rotated over the polar and azimuth angles, ψ and φ, and the intensity is recorded (Figure 2.6). The measurements are carried out on a specific pole of the crystal and this is the reason why it is called a *pole* measurement. Under the assumptions that the specimen is infinitely thick and the grain size is the same for all oriented grains and after background and defocus corrections, the intensity can be interpreted as a relative crystal distribution. There is, however, still a rotational degree of

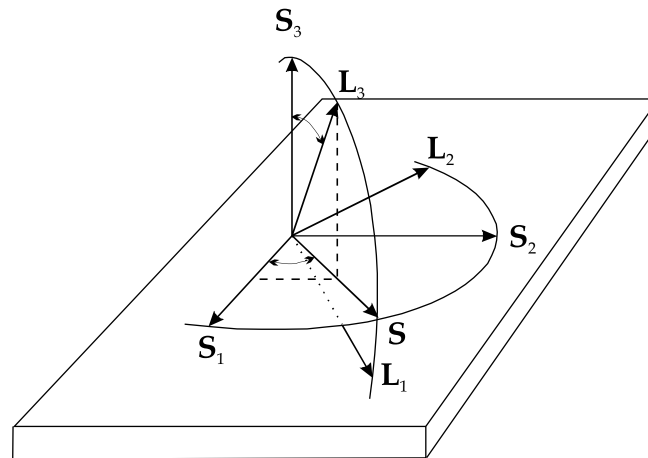

Figure 2.6 Relation between the specimen system defined by the orthogonal vectors $\mathbf{S}_1$, $\mathbf{S}_2$ and $\mathbf{S}_3$ with $\mathbf{S}_1$ and $\mathbf{S}_2$ in the plane of the specimen and the laboratory system fixed by the orthogonal vectors $\mathbf{L}_1$, $\mathbf{L}_2$ and $\mathbf{L}_3$ with $\mathbf{L}_3$ perpendicular to the planes in the reflecting grains expressed in the angles and .

freedom around the axis perpendicular to the axis of diffraction. Therefore, to get a clear picture of the orientation of the crystallites it is necessary to perform measurements on different lattice planes. With three pole figures obtained using X-ray diffraction it is possible to calculate the unambiguous orientation distribution of the crystals, i.e. the orientation distribution function, ODF.

There are situations conceivable where it is not possible to execute the texture measurements as depicted above. When for example the substrate reflections interfere with the reflections of a film. However, it is still possible to acquire some information about the alignment of the crystals. The integrated intensity obtained from X-ray measurements can be compared with the integrated intensity of a powder specimen of the same material. The difference is a consequence of preferential alignment of the crystals and it is thus possible to determine which crystallographic plane is preferentially oriented parallel to the surface.

2.2.4 X-rays and macro residual stresses

Extrinsic or intrinsic forces working on matter will result in a deformation of this matter. When the external forces are removed the deformation, assuming it was within the elastic range, will disappear as well. However this is not the case for the internal force, as they bring about a permanent deformation, i.e. a permanent stress, which is better known as *residual stress* [7,20]. The residual stresses, which are inherent in the material, are divided into three groups:

- Macro residual stress, RS1.
- Micro stress, RS2.
- Micro stress, RS3.

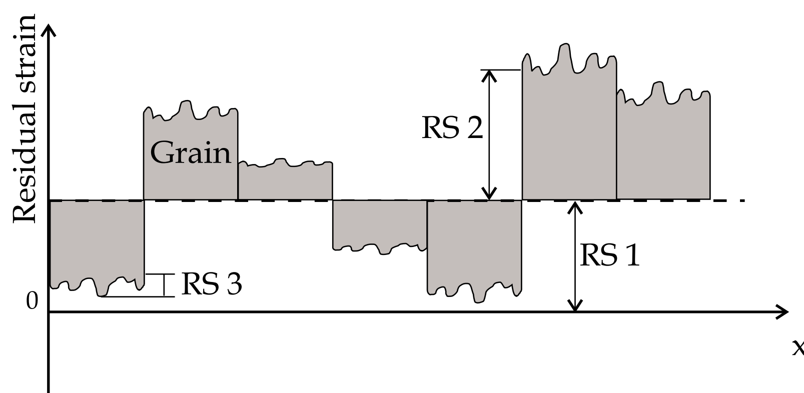

Figure 2.7 The three types of residual stresses.
RS1 is the macroscopic stress in the specimen. RS2 is the average micro stress in a grain and RS3 is the variation in micro stress within a specific grain.

This division is pictured in Figure 2.7, which shows that the residual stress in crystalline materials may vary from one part of the grain to another part, RS3, and between different grains, RS2. However, over large distances the stress may be quite uniform resulting in the macroscopic stress, RS1. The influence residual stresses have on the diffraction depends on the specific group it belongs to. *Macro residual stresses* will result in a shift of the diffraction peak as the lattice spacing of a grain is altered and the diffraction condition is fulfilled at a different 2θ. The change in stress within a grain will result in a diffraction condition depending on the position within the grain. It appears to be composed of sub grains resulting in a peak broadening. This is also called the *deformation strain* which term will be used in the remainder of this thesis. The precise influence of the deformation strain and the grain size on the profile of the diffraction peaks will be discussed in the next section.

To be able to determine the macro residual stresses in a specimen a procedure similar to the texture measurement must be executed. When in a certain direction, defined by a polar and azimuth angle, the peak position is determined the strain can be calculated with:

$$\varepsilon^{lab}_{\varphi\psi\{hkl\}} = \frac{d_{\varphi\psi\{hkl\}} - d_0}{d_0} \tag{2.12}$$

This is the strain in the laboratory system of the diffractometer and has to be transformed to the strain matrix of the specimen system. This is readily obtained by taking the directional cosines of the strain components in the specimen system:

$$\begin{aligned} \varepsilon^{lab}_{(\varphi,\psi)} = {} & \varepsilon_{11}\cos^2\varphi\sin^2\psi + \varepsilon_{12}\sin 2\varphi\sin^2\psi + \varepsilon_{22}\sin^2\varphi\sin^2\psi \\ & + \varepsilon_{33}\cos^2\psi + \varepsilon_{13}\cos\varphi\sin 2\psi + \varepsilon_{23}\sin\varphi\sin 2\psi \end{aligned} \tag{2.13}$$

When all the components of the strain matrix are non-zero, i.e. triaxial strain state, it is compulsory to determine the lattice spacing as a function of ψ in three different φ directions: at 0, 45 and 90 degrees. For the relatively thin films considered in this thesis the situation can be simplified considerably. The strain in thin films is biaxial, so ε_{13} and ε_{23} are zero and it is only necessary to determine the relation between the lattice spacing and the ψ in two φ directions 90° apart. With the strain tensor disentangled it is possible to calculate the residual stresses. This is far from a straightforward procedure and is discussed in more depth in section 2.3. It is worthwhile to mention that in Equation (2.12) the empirical $d_{\varphi\psi}$ is a mean value and in order to make the equation flawless it must be substituted by $\langle d_{\varphi\psi} \rangle$.

Displacement of the specimen from the diffractometer axis may have a large influence on the determinations of the macro residual stresses. The influence of this becomes apparent when we consider the influence of a ψ tilt on the error in the lattice spacing. Equation (2.11) is now changed into:

$$\frac{\Delta d}{d} = -\frac{D}{R} \cdot \frac{\cos^2 \theta}{\sin \theta \cdot \cos \psi} \tag{2.14}$$

The additional term $1/\cos\psi$ will increase the error considerably and will change the linear d-$\sin^2\psi$ graph into a curved one. In Table 2.4 the influence of the ψ tilt on a pre-existing displacement error, 10 µm at ψ=0, on the lattice spacing of three different planes is calculated. It is clear from these numbers that the ψ tilt can result in a significant influence on the measured d spacings, especially for small angle reflections and larger ψ's. So an error in the height may result in a curved d-$\sin^2\psi$ relation.

Table 2.4 Influence of the ψ tilt on the error in the lattice spacing.

		Δd [Å]	
ψ [°]	{111} θ=18.34°	{200} θ=21.30°	{400} θ=46.61°
0	0.0004	0.0002	0.0001
30	0.0005	0.0004	0.0001
45	0.0006	0.0005	0.0001
60	0.0008	0.0007	0.0002

2.2.5 X-rays, grain size and deformation strain

The size of and imperfections within a grain will have an effect on its diffraction pattern [18,19,21] but is it possible to separate and determine these two effects?

Grain size

The starting point is a perfect cubic crystal that is fulfilling the diffraction condition of Equation (2.7). What will happen if the directions are slightly altered? The diffraction for two adjacent planes is no longer fulfilled because we have introduced an additional path difference, Δs, between the two planes.

$$\vec{s}_d - \vec{s}_p - \Delta\vec{s} = \lambda\left(h\vec{a}_1 + k\vec{a}_2 + l\vec{a}_3\right) \tag{2.15}$$

However, the difference between plane x and plane $x+n$ is n times this path difference and when this is equal to half a wavelength destructive interference will occur for these two rays. So when the size of a crystal is infinite this will

occur for all non-ideal rays and the diffraction peaks are very sharp. Decreasing the crystal size will result in diffraction broadening because when there are only *n-1* planes this difference of half a wavelength will not be reached. This broadening depends on the distance between the planes and is thus different for different {hkl} reflections. This is described by the Scherrer equation.

$$\beta = \frac{K\lambda}{L\cos\theta} \tag{2.16}$$

Where β is the width of the diffraction peak in radians, L is the size of the grain and K is a factor, which depends on the shape assumed for the intensity distribution of diffraction. Its value is close to unity.

Deformation strain

In a distorted crystal the structure amplitude of the unit cell originally at **r** will differ from that at the origin. This is due to two effects:

- The cell is displaced (rigid body translation)
- It undergoes a rotation.

This rotation may be neglected because it is small compared to the displacement. This results in an adapted structure factor of the unit cell at **r**:

$$F' = F\mathrm{e}^{-2\pi i\left(h\vec{b}_1 + k\vec{b}_2 + l\vec{b}_3\right)\cdot\vec{u}} \tag{2.17}$$

where **u** is displacement and the **b**s are the edges of the unit cell of the reciprocal lattice.

The product of the structure amplitudes of two cells separated a distance *t* can now readily be obtained. Under the assumption that the distortion in the unit cells is non-periodic, this results in a structure amplitude for the crystal given by:

$$J = FF^{*}\,\overline{\mathrm{e}^{2\pi i\cdot t\cdot\left(h\vec{b}_1 + k\vec{b}_2 + l\vec{b}_3\right)\cdot\nabla\vec{u}\cdot\frac{h\vec{b}_1 + k\vec{b}_2 + l\vec{b}_3}{\left|h\vec{b}_1 + k\vec{b}_2 + l\vec{b}_3\right|}}} \tag{2.18}$$

In this equation **∇u** is the tensor of which the symmetrical part is the engineering strain tensor e_{ij} and the anti-symmetrical part is the rotation tensor.

So the tensile strain in the {hkl} direction can be introduced and integrating Equation (2.18) with respect to the strain and the distance results in the strain broadening (i.e. micro stress broadening).

$$\beta \cot\theta = \frac{2}{\phi_{hkl}(0)} \tag{2.19}$$

where β is the broadening and ϕ_{hkl} is the distribution of the strain in the crystal. The problem of calculating the broadening is thus reduced to the problem of calculating the distribution of the tensile strain in the {hkl} direction of the crystal. The approximation that all values of e_{hh} between zero and a maximum are equally likely, $\phi(0)=½(e_{hh})_{max}$, results in:

$$\beta = 4 e_{hh}^{\max} \tan\theta \tag{2.20}$$

The profile obtained is a convolution of the functions representing the different broadening effects. Besides the broadening due to size and micro-stress effects there is always extraneous broadening due to non-monochromatic radiation, slit sizes and an imperfect focus. This broadening is called the instrumental broadening. Assuming the profiles of the different contributions have a Gaussian or Cauchy shape, results in an attractive relation between the half maximum breadths of the curves:

$$\begin{aligned} i &= I\exp^{-\frac{4\log ½}{\beta^2}x^2} & \beta_t^2 &= \beta_{instrumental}^2 + \beta_{grain}^2 + \beta_{strain}^2 \quad (a) \\ i &= \frac{I}{1+\frac{2}{\beta^2}x^2} & \beta_t &= \beta_{instrumental} + \beta_{grain} + \beta_{strain} \quad (b) \end{aligned} \tag{2.21}$$

However, the curves are never pure Gaussian or Cauchy and this will introduce an error in the determined grain size and micro stress.

Leaving out the instrumental broadening makes it possible to rewrite Equation (2.21) with Equations (2.16) and (2.20):

$$\begin{aligned} &\textit{Gaussian} & \beta_t^2 &= \frac{K^2\lambda^2}{L^2\cos^2\theta} + 16(e_{hh}^{\max})^2\tan^2\theta \quad (a) \\ &\textit{Cauchy} & \beta_t &= \frac{K\lambda}{L\cos\theta} + 4e_{hh}^{\max}\tan\theta \quad (b) \end{aligned} \tag{2.22}$$

Equation (2.22) is rewritten into:

$$\frac{\beta_t\cos\theta}{\lambda} = \frac{K}{L} + 4e_{hh}^{\max}\frac{\sin\theta}{\lambda} \tag{2.23}$$

When $\beta{\cdot}\cos\theta/\lambda$ is plotted as a function of $4\sin\theta/\lambda$, called a Williamson-Hall plot [22], it is possible to determine the grain size and the deformation strain because the reciprocal of the intercept gives the grain size and the slope of the line is due to strain broadening. So separation of the finite grain size and strain

broadening is possible but is certainly not a method that should be applied without critical evaluation.

2.3 Stress calculations

It was shown in section 2.2.4 that X-rays can be used to determine the long-range strain that is present in a material. However, in general one is interested in the long-range stresses, i.e. the macro residual stresses. To calculate the stress from the strain it is necessary to perform a transformation [20,23]:

$$\begin{aligned}\varepsilon^{lab}_{\varphi\psi\{hkl\}} &= \tfrac{1}{2}S_2^{hkl}\left(\sigma_{11}\cos^2\varphi+\sigma_{12}\sin 2\varphi+\sigma_{22}\sin^2\varphi-\sigma_{33}\right)\sin^2\psi \\ &+\tfrac{1}{2}S_2^{hkl}\sigma_{33}+S_1^{hkl}\left(\sigma_{11}+\sigma_{22}+\sigma_{33}\right)+\tfrac{1}{2}S_2^{hkl}\left(\sigma_{13}\cos\varphi+\sigma_{23}\sin\varphi\right)\sin 2\psi\end{aligned} \tag{2.24}$$

For isotropic linear elastic materials, the reflection indices disappear and the X-ray elastic constants, XEC, are in terms of the Poisson's and the Young's modulus.

$$\begin{aligned} S_1 &= \frac{-\nu}{E} && (a) \\ \tfrac{1}{2}S_2 &= \frac{1+\nu}{E} && (b)\end{aligned} \tag{2.25}$$

However, the mechanical properties are on the level of a single crystal always anisotropic and results in a more complicated relation between stress and strain than the familiar Hooke's law. Both the stress and the strain are second rank tensors and a transformation matrix containing 81 components relates them. For anisotropic cubic materials, only three of these 81 components are independent, S_{11}, S_{12} and the S_{44}. The XEC can be calculated with these elastic compliances when the crystallographic orientation of the specimen is known and an interaction model is chosen. These two facts can be taken into account by starting with the adapted stress-strain relation [24]:

$$\begin{aligned}\left\langle \varepsilon^{lab}_{\varphi\psi\{hkl\}}\right\rangle &= \left(\left\langle s^{lab}_{33ij}\right\rangle+\left\langle t^{lab}_{33ij}\right\rangle\right)\left\langle \sigma_{ij}\right\rangle && (a) \\ r^{lab}_{ij} &= \left\langle s^{lab}_{33ij}\right\rangle+\left\langle t^{lab}_{33ij}\right\rangle && (b)\end{aligned} \tag{2.26}$$

$\langle\sigma_{ij}\rangle$ is the average stress over the penetration depth. The $\langle s^{lab}_{33ij}\rangle$ is the compliance and $\langle t^{lab}_{33ij}\rangle$ is the interaction term representing the coupling of a grain with the surrounding matrix. This coupling depends on the XEC and the crystallographic texture, both in the laboratory system.

Quasi isotropic

For a quasi-isotropic specimen, the orientation of the axis of the laboratory system is irrelevant. Equation (2.26) can be used directly and it is only necessary to omit the superscript *lab* in the compliance and the interaction terms. For the quasi-isotropic approach r_{12}, r_{13} and r_{23} are zero.

Neglecting the interaction term leaves two possible assumptions:

- The strain is constant, Voigt average.
- The stress is constant, Reuss's approximation.

This is clear from Figure 2.8, which shows two grains with a different orientation. When they are connected to a wall applying a force in the x direction will result in a constant stress in both grains but this means that the strain is not the same in both grains. However connecting both materials to a substrate, which is stretched, will result in an equal deformation of the grains, constant strain, but now the stress in both grains is different.

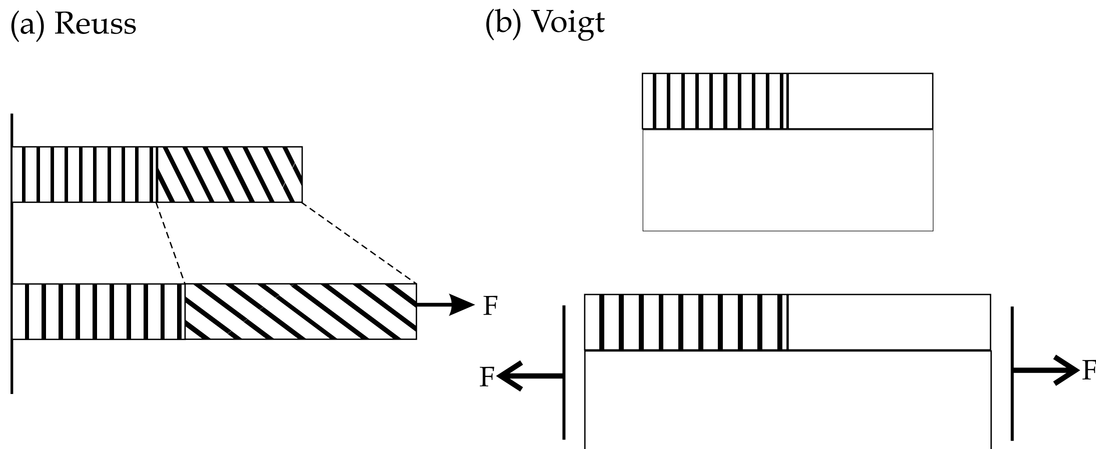

Figure 2.8 Assuming constant stress, Reuss's approximation, results in a different strain due to a difference in Young's moduli. The opposite case is imposing a defined strain which results in the Voigt model.

Using Voigt's approximation will result in a constant S_1 and $\frac{1}{2}S_2$ but the XEC derived from the Reuss average will depend on the reflection indices {hkl} and are:

$$S_1^{hkl} = S_{12} + s_0 \tag{2.27}$$

$$\tfrac{1}{2}S_2^{hkl} = S_{11} - S_{12} - 3s_0\Gamma \tag{2.28}$$

With

$$s_0 = S_{11} - S_{12} - \tfrac{1}{2} S_{44} \tag{2.29}$$

$$\Gamma = \frac{h^2k^2 + h^2l^2 + k^2l^2}{(h^2 + k^2 + l^2)^2} \tag{2.30}$$

For the Reuss and Voigt models the interaction term was neglected but when the crystal interaction is taken into account the outcome is a solution which will lie somewhere in between the outcome of the Reuss and the Voigt approach. This is visible from Figure 2.9 that shows the XEC according to the models stated above and an additional model considering the grain interaction, this is called Kröner's model, plotted as a function of Γ.

What is the exact influence of the three models described above on the stress calculations? Basically there is no influence on Equation (2.24) as only the values used for the XEC will vary and they act as a kind of scaling. The only important point is the stress tensor used. It is clear from Equation (2.24) that when the measured <d> is plotted versus $\sin^2\psi$ this yields a linear relation, when the shear stresses σ_{13} and σ_{23} are zero (2ψ dependency). In general, even

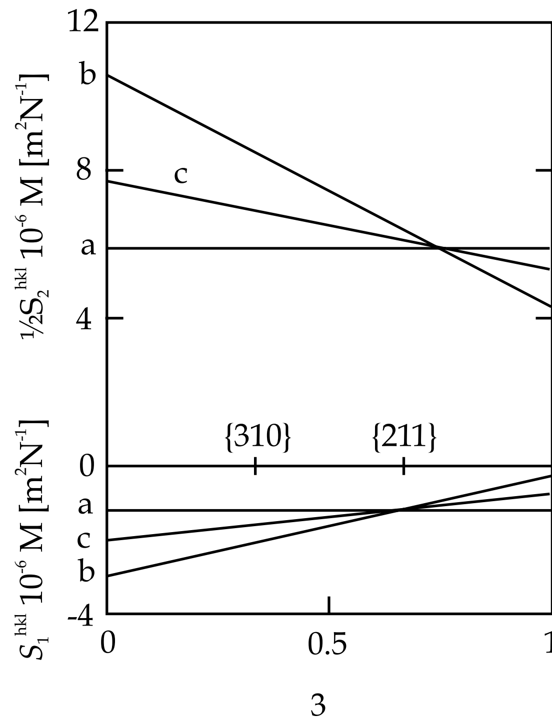

Figure 2.9 The XEC are plotted as a function of the used {hkl} planes. The used approximation, (a) Voigt, (b) Reuss or an intermediate model Kröner (c), results in a different relation between the X-ray elastic constants and the reflections.

when these shear stresses are non-zero, the measurements are represented in this way and this is known as the ***d-sin²ψ method***. The presence of σ_{13} and σ_{23} will result in a different d-$\sin^2\psi$ relation for $\psi>0$ and $\psi<0$. This is called ψ splitting and is easily detectable.

Textured specimen

For a textured specimen Equation (2.26) cannot directly be used and a new factor is defined:

$$R^{lab}_{ij\varphi\psi\{hkl\}} = \frac{\lambda^{random} \Gamma^{hkl}_{ij} + \lambda^{ODF} \left\langle s^{lab}_{33ij} \right\rangle^{ODF}}{\lambda^{random} + \lambda^{ODF}} \tag{2.31}$$

When there are no random grains then λ^{random} is zero which results in the single crystal compliances. The opposite case, no preferred orientation that is $\lambda^{ODF}=0$, results in the Reuss XEC. (The $<s_{33ij}>$ in the laboratory system is the average value over the different crystallographic directions.)

The texture will change the relation between the strain in the laboratory and the stress in the specimen system and applying the d-$\sin^2\psi$ method will, normally, result in a relation that is non-linear, which complicates the stress analysis. Normally, means in this case that the s^{lab}_{3312}, s^{lab}_{3313} and s^{lab}_{3323} are non zero. However, for cubic material there are two planes for which these three values are zero, the {h00} and the {hhh} planes. Measurements on these planes show the same behaviour as that of the quasi-isotropic approach and thus a linear d-$\sin^2\psi$ relation.

2.4 Scanning electron microscopy

The resolving power of a microscope depends to a certain extent on the wavelength of the used radiation. In some cases it is possible to increase this resolving power with special technique like for example a confocal microscope but the easiest way is to use radiation with a shorter wavelength. This has resulted in the birth of the electron microscopy and the first electron microscope was fabricated in 1932 [25]. There are two types of electron microscopes:

- Microscopes which scan the surface of a specimen with an electron beam, scanning electron microscope called *SEM* hereafter.
- Transmission microscopes, *TEM*, where the electron beam is transmitted through a thin specimen and is collected underneath the specimen.

In this thesis only the SEM is used for investigation of the deposited coatings.

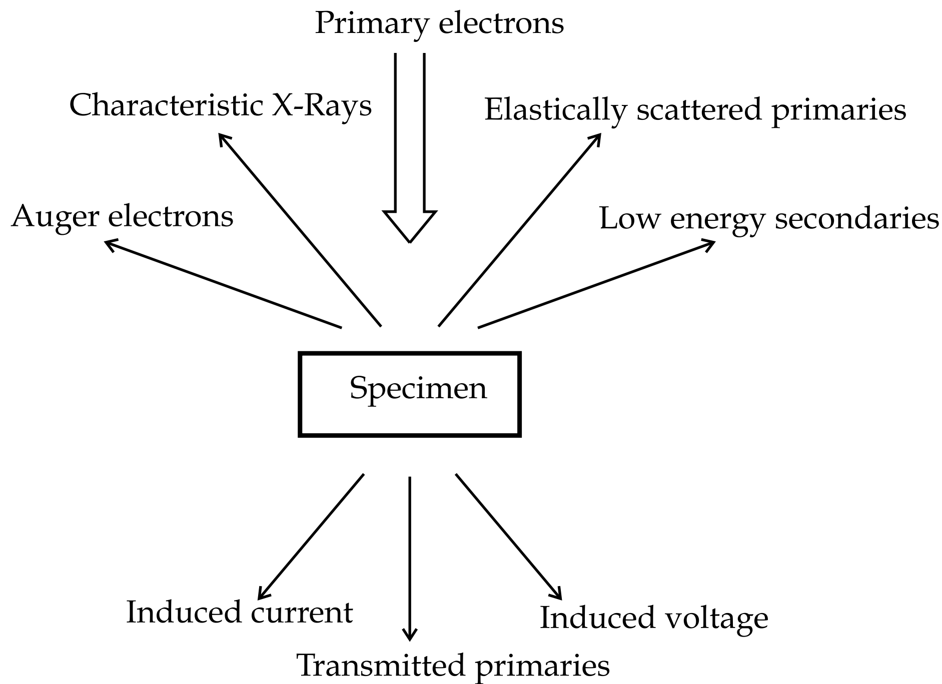

Figure 2.10 The interaction of an electron beam with matter result in Auger electrons and X-rays which can be used for the characterization of the specimen and the elastically scattered and secondary electrons which are used for visible imaging of the specimen.

Principle of an SEM

The interaction of a high energy electron, primary electron, with the assembly of electrons in a solid depends not only on the precise energy of the primary electron but also on numerous other aspects and can be dealt with only on a statistical basis. The most commonly arising effects are shown schematically in Figure 2.10. Not all these effects may be large enough to be detectable. However, virtually all materials will exhibit usefully large secondary electron currents and X-ray emissions.

The electrons that leave the specimen can be divided in four groups (Figure 2.11):

1. Primary electrons, which have undergone a few large angle elastic collisions, without an appreciable loss of energy.
2. In-elastically scattered primary electrons, called back-scattered electrons.
3. Auger electrons.
4. Finally, the majority of electrons with energies between 0 and 50 eV, called the secondary electrons.

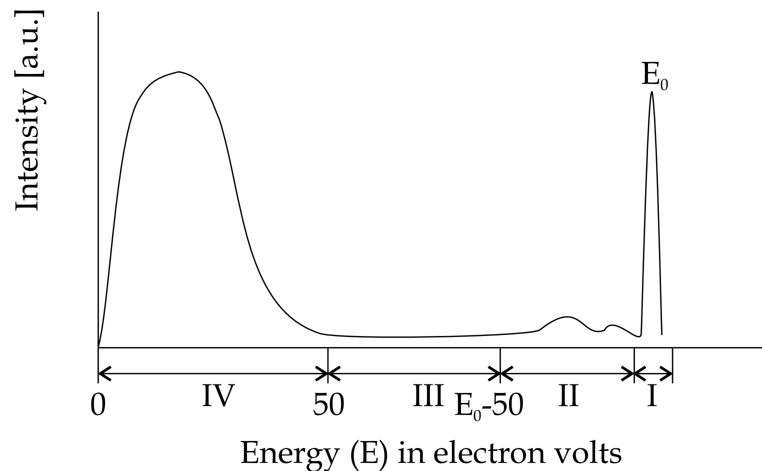

Figure 2.11 Energy spectrum of the electrons leaving the specimen. Region I contains the high energy elastically scattered primary electrons. Region II contains the back-scattered primary electrons. In region III the Auger electrons are situated, between 100 and 1000 eV. Region IV contains the secondary electrons.

This secondary emission current strongly depends on the workfunction of the material, a higher workfunction means higher emission, and this difference in emission for different materials is an important source of contrast.

The scanning electron microscope has numerous advantages:

- The great depth of focus in comparison with an optical microscope.
- The possibility of direct observation of the external form of real objects, such as complex fracture surfaces at high magnification.
- The large space available for dynamic experiments on the specimen.

The fast developments in the electron microscope area have considerably reduced the disadvantages of a decade ago. The lack of resolution is solved with a field emission gun, FEG, filament and the limitations of the vacuum environment are solved in the environmental SEM, *E-SEM*, by pressure limiting apertures.

When in-situ experiments, as for example bending and tensile tests, are carried out in an SEM it is possible to obtain valuable information about mechanical properties of a coating. Bending experiments are carried out in an environmental SEM on the three commercial systems, TiN, Ti(C,N) and TiN/TiAlN. In the used bending stage, see Figure 2.12, three and four point bending experiments can be carried out with the coating loaded in compression or in tension. For the bending tests under tension, the specimen can be studied

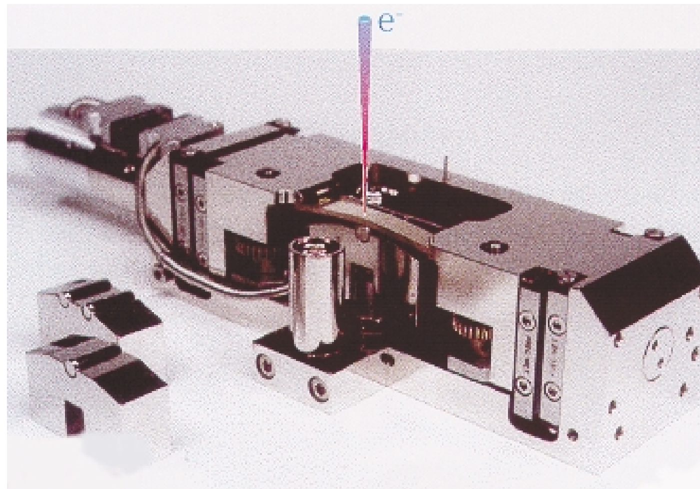

Figure 2.12 Bending stage of the environmental SEM

in cross section and in the top view mode. For the compressive tests only the cross section of the coatings can be investigated.

Chemical characterisation

If an electron is exited to leave an atom or to go into a higher unoccupied level an electron hole is formed. This electron hole is filled by one of the outer shell electrons, conserving energy by emitting an X-ray photon. This X-ray spectrum is unique to each element and therefore an analysis of the X-ray emission of any specimen can give an analysis of the constituent elements in the specimen. The information depth of X-ray emission depends on the energy of the primary electrons and the elements in the specimen, but is, for solids, generally of the order of micrometers. This technique has one disadvantage, namely it is not very suitable for lighter elements.

Closely related to X-ray emission is the emission of Auger electrons since it begins also with the ejection of an electron from an inner atomic shell. The photon that is generated when this hole is filled is absorbed by another electron and the process ends with the emission of this electron with an energy, which is related to the allowed electron energy in the atom. The short free path length of Auger electrons, which limit the escape depth of the electrons, makes Auger spectroscopy a surface sensitive technique and ideal to study the composition of ultra thin layers.

References

1 R.W. Berry, P.M. Hall, M.T. Harris, Thin film technology, D. van Nostrand inc., Princeton, 1968.
2 D.L. Smith, Thin Film Deposition: Principle & Practice, Mc Graw Hill, New York, 1995.
3 Private communications with D. Tran of the Technical University of Eindhoven.
4 W.G. Moffatt, Binary phase diagrams handbook, Genium Publ. Corp., Schenectady New York, 1984.
5 E. Vogelzang, J. Sjollema, H.J. Boer, J. Th. M. De Hosson, J. Appl. Phys. 61(9) (1987) 4606.
6 J.O. Kim, J.D. Achenbach, J. Appl. Phys. 72 (5) (1992) 1805.
7 B. Eigenmann, E. Macherauch, Mat. –wiss. U. Werkstofftech. 26 (1995) 199.
8 A.J. Perry, Thin Solid films 193/194 (1990) 463.
9 E. Zoestbergen, J. Th. M. De Hosson, Thin Solid Films 371 (2000) 10.
10 A.D. Mc Quillan, M.K. McQuillan, Titanium, Butterworths Scientific Publications, London 1956.
11 Gmelin Handbook of Inorganic Chemistry, Springer, Berlin (1982) 44.
12 Handbook of Chemistry and Physics, CRC Press Inc., Boca Raton Florida, 63ed. 1982-1983.
13 A.B. Kloosterman, Surface Modifications of Titanium with Lasers, Groningen University Press, Groningen (1998).
14 K.H. Kim, S.H. Lee, Thin Solid films 283 (1996) 165.
15 K.N. Andersen, E.J. Bienk, K.O. Schweitz, H. Reitz, J. Chevallier, P. Kringhoj, J. Bottiger, Surf. Coat. Technol. 123 (2000) 219.
16 D.Y. Wang,C.L. Chang, K.W. Wong, Y.W. Li, W.Y. Ho, Surf. Coat. Technol. 120-121 (1999) 388.
17 B.E. Warren, X-ray Diffraction, Dover Publications INC. New York 1990.
18 B.D. Cullity, Elements of X-ray diffraction, Addison-Wesley, Reading, Massachusetts, 1978.
19 E.F. Kaelble, Handbook of X-rays, McGraw-Hill, New York, 1967.
20 I.C. Noyan, J.B. Cohen, Residual stress, Springer-Verlag Inc., New York, 1987.
21 A.R. Stokes, A.J.C. Wilson, Proc. Phys. Soc. 56 (1944) 174.
22 G.K. Williamson, W.H. Hall, Acta Metall. 1 (1953) 22.
23 V. Hauk, H.J. Nikolin, Textures and microstructures 8/9 (1988) 693.
24 H. Dölle, J, Appl. Crystallogr. 12 (1979) 489.
25 J.W.S. Hearle, J.T. Sparrow, P.M. Cross, The use of the scanning electron microscope, Pergamon Press Oxford, 1972.